The Journal of the Acoustical Society of America

OCTOBER 11 2024

Phase stability of convergence zone propagation at mid-frequency

F. Hunter Akins ; William S. Hodgkiss; W. A. Kuperman

J. Acoust. Soc. Am. 156, 2409–2421 (2024)
https://doi.org/10.1121/10.0032359

JASA ARTICLE

Phase stability of convergence zone propagation at mid-frequency

F. Hunter Akins,[a] William S. Hodgkiss, and W. A. Kuperman
Scripps Institution of Oceanography, University of California San Diego, La Jolla, California 92093, USA

ABSTRACT:
Mid-frequency transmissions (1.5 to 7.5 kHz) from a towed source to a drifting array one convergence zone away demonstrate smoothly varying phase. Calculations of the strength and diffraction parameters Φ and Λ for a representative background environment predict partially saturated propagation. For a single convergence zone path, the evolving phase rate due to the changing internal wave field corresponds to a narrowband coherent integration time, defined by the length of a discrete Fourier transform that likely captures the signal, from ∼370 s at 10 kHz to ∼1370 s at 1 kHz in the absence of source motion. Simulated propagation with a split-step parabolic equation solver through a sound speed field with thermocline fine structure and a Garrett-Munk internal wave displacement field provides a full wave picture that is consistent with the statistical predictions. Experimental data from the Philippine Sea demonstrates signal phase that is highly correlated with source tow body vertical excursions, measured by a pressure sensor, that couple into horizontal motion. The received signal can be integrated for up to 128 s at 5.5 kHz, with the upper limit thought to be due to non-uniform source motion rather than ocean dynamics.
 https://doi.org/10.1121/10.0032359

(Received 17 May 2024; revised 27 August 2024; accepted 22 September 2024; published online 11 October 2024)

[Editor: John A. Colosi] Pages: 2409–2421

I. INTRODUCTION

Phase stability is an important signal quantity for passive sonar applications and underwater communications. The source frequency and acoustic propagation transfer function (which includes multipath and boundary interactions) determine the sensitivity of the measured acoustic field and its stability to ocean dynamics. This work analyzes propagation at mid-frequency from a shallow source to a shallow receiver in a convergence zone (CZ). Theoretical results indicate that the 60 km propagation paths, though strongly dependent on the ocean conditions, vary slowly with time, and support integration times of approximately 370 to 1370 s even at mid-frequency (1–10 kHz). Acoustic data collected on a 64-element vertical line array (VLA) from a source tow during a deep water experiment in the Philippine Sea demonstrates smoothly varying phase. The nonlinear component of the phase evolution (i.e., the phase time series with its linear trend removed) is highly correlated with pressure sensor measurements on the source tow body for segments up to 210 s. Increasing signal-to-noise ratio (SNR) can be obtained for DFT lengths up to 128 s.

Hale[1] provides a review of the early history of CZ research as well as an analysis of CZ propagation using ray theory. In a study on CZ spatial coherence, Urick and Lund[2] measured the correlation coefficient of the pressure field at vertically separated hydrophones up to 4.572 m apart from a shallow 1120 Hz source and found that CZ propagation had high spatial coherence compared with non-CZ propagation. A number of recent studies apply numerical models to examine the sensitivity of CZ propagation to sound speed profile (SSP) characteristics.[3–5] This work analyzes the effect of ocean dynamics, primarily internal waves, on the phase stability of mid-frequency transmissions in a CZ and compares the theoretical predictions to observations of phase.

The theory of wave propagation in random media (WPRM),[6] first tailored to the ocean acoustic problem by Munk and Zachariasen,[7] predicts different propagation regimes depending on the strength of random scattering along propagation paths.[8,9] The book of Colosi is an up-to-date reference for WPRM in underwater acoustics.[10] Application of WPRM theory to CZ propagation relevant for the experimental data predicts propagation in the partially saturated regime. In contrast with full saturation, a regime in which the phase becomes randomized, the partial saturation regime predicts a smoothly evolving phase and relatively stable amplitude. WPRM theory is also used to compute the phase rate autocorrelation function for a single CZ eigenray in a Garrett-Munk internal wave field, which is then related to the expected coherent integration time of a narrowband signal.

A simulation applying the split-step parabolic equation solver to a time- and range-dependent sound speed field allows for a rough evaluation of multipath effects present in the data on phase stability. The simulation results are consistent with WPRM theory and indicate that multipath interference in the CZ does not significantly degrade the integration time. The synthetic sound speed field includes fine structure in the thermocline near the upper turning points (100 to

[a]Email: fakins@ucsd.edu

300 m depth) using the Poisson model of Pinkel[11] and uses a Garrett-Munk excited internal wave displacement field to displace the water.

Predictions are compared to experimental data collected in the Philippine Sea on a 64-element VLA. The received signal phase in a CZ at 1.5 to 5.5 kHz, measured in a broad horizontal beam, varies smoothly but has a significant non-linear component. For segments of data up to 210 s, the non-linear component of phase is highly correlated with pressure sensor measurements on the source tow body. The simulations and WPRM results predict integration times of approximately 500 s for a stationary source at 5.5 kHz. In the data, at 5.5 kHz, signal gain was obtained on segments up to 128 s and thought to be limited by non-uniform source motion (non-constant range-rate and depth) as opposed to ocean dynamics.

The paper is organized as follows. The experiment geometry is described in Sec. II. A definition of phase rate coherence time relevant for narrowband passive processing is provided in Sec. III. Analysis of CZ propagation using a smoothed background sound speed profile, including calculations of the strength and diffraction parameters as well as travel time statistics, is presented in Sec. IV. A single simulation with internal waves and thermocline fine structure for a 5.5 kHz source is presented in Sec. V to address the effects of multipath interference from a dynamic ocean and moving source. Data from a source tow is analyzed in Sec. VI. The received signal phase measured in a beam is compared to measurements of a pressure sensor on the source tow body. The coherent gain obtained by integrating the signal in a beam is shown for increasing DFT length. Conclusions are provided in Sec. VII. Appendix A describes the traditional definition of coherence time in terms of the mutual coherence function and compares it to the phase rate coherence time definition of Sec. III. Appendix B provides the necessary information for the strength and diffraction parameter calculations. Appendix C details the calculation of travel time statistics used to compute the phase rate coherence time in Sec. III. Appendix D describes the sound speed profile simulation method used in Sec. V.

II. EXPERIMENT GEOMETRY

The experiment took place in deep water in the Philippine Sea. A 64-element vertical line array (VLA) with an element spacing of 1/8 m ($\lambda/2$ at 6 kHz) measured the acoustic field. The array was tethered to a buoy and drifted at a depth of 143 m.

The transmission event analyzed here took place during a 9 h source tow in which the source closed in on the drifting array at a mean range-rate of 1 m/s, shown in Fig. 1. During this 9 h period approximately 65 min (corresponding to a 4 km extent) were spent in the CZ, which is easily identified by the increased signal level and characteristic arrival pattern. The source is towed at a depth of approximately 150 m. Due to drag on the tow body and cable, the source does not hang directly beneath the ship. Rather it follows some distance behind the ship and moves along the local catenary of the tow cable in response to changes in ship speed and heave. The angle of the tow cable at the source is estimated to be inclined at 50° to 70° with respect to the horizontal in Sec. VI. The water depth at the midpoint between source and receiver was approximately 4700 m during the CZ segment.

III. PHASE RATE COHERENCE TIME

The precise definition of coherence varies depending on the context and the application under consideration (for a historical evolution and consideration in the context of acoustics, the reader is referred to Ref. 12) This section defines a phase rate coherence time relevant for narrowband filtering on a single ray arrival. A discussion of the relationship between the traditional coherence time in terms of the mutual coherence function and the phase rate coherence time defined here is provided in Appendix A.

A. Evolving phase rate

This section defines a phase rate coherence time that quantifies the narrowness of a filter that can be applied to a sinusoidal transmission to obtain gain over noise. To be precise, we take the filter to be the output in a single bin of the discrete Fourier transform (DFT) applied to T seconds of data with a rectangular window. The passband for this filter, defined as the bin width, is $1/T$ Hz.

The instantaneous received signal frequency $f_r(t)$ (the phase rate) from a stationary source with frequency f_0 to a stationary receiver along a ray path with an evolving travel time $\tau(t)$ is

$$f_r(t) = f_0(1 - \dot{\tau}(t)), \tag{1}$$

where $\dot{\tau}(t)$ is the travel time rate of change.

Assume that the travel time rate of change $\dot{\tau}(t)$ is a zero mean stationary Gaussian process whose autocorrelation

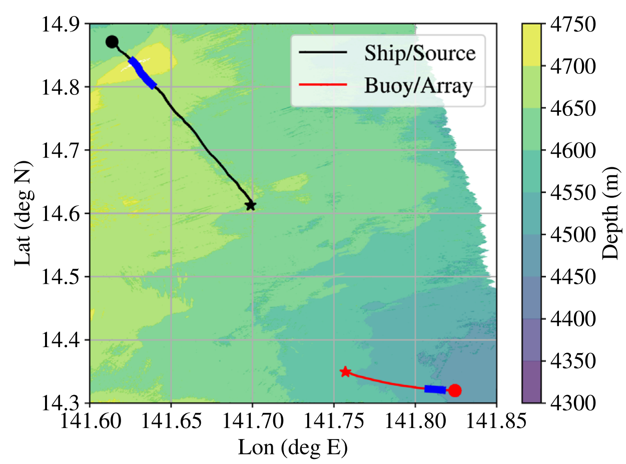

FIG. 1. (Color online) The full 9 h source tow track shown over bathymetry collected by the multibeam system on the R/V Sally Ride during the experiment. The start of paths is marked with a dot and the end of paths is marked with a star. The approximately 65 min CZ portion is highlighted in blue.

function depends on the ray path under consideration, the buoyancy profile of the environment, and the Garrett-Munk internal wave spectrum shape. Then the travel time rate of change autocorrelation function $R_{\dot{\tau}}(t,t')$ depends only on the time separation $T = t - t'$,

$$R_{\dot{\tau}}(T) \equiv \langle \dot{\tau}(t+T)\dot{\tau}(t) \rangle, \tag{2}$$

where $\langle \cdot \rangle$ denotes expectation over internal wave realizations. Under this assumption, the difference in received frequency from transmitted frequency

$$\Delta f(t) \equiv f_0 \dot{\tau}(t) \tag{3}$$

is also a zero mean stationary Gaussian process with autocorrelation function

$$R_{\Delta f}(T) = f_0^2 R_{\dot{\tau}}(T). \tag{4}$$

Define the random variable $\Delta\nu(t, t+T)$ to be the change in received frequency between two fixed times t and $t+T$,

$$\Delta\nu(t, t+T) = \Delta f(t+T) - \Delta f(t). \tag{5}$$

Because Δf is a zero mean random process, $\Delta\nu$ is zero mean for any t and T. The variance of $\Delta\nu$ is

$$\sigma^2_{\Delta\nu}(t, t+T) = \langle \Delta f^2(t) \rangle + \langle \Delta f^2(t+T) \rangle - 2\langle \Delta f(t)\Delta f(t+T) \rangle. \tag{6}$$

Recognizing that $\langle \Delta f^2(t) \rangle = \langle \Delta f^2(t+T) \rangle = R_{\Delta f}(0)$, $\langle \Delta f(t)\Delta f(t+T) \rangle = R_{\Delta f}(T)$, and using Eq. (4), the variance of the change in received frequency $\Delta\nu$ can be written in terms of the travel time rate of change autocorrelation function and the source frequency

$$\sigma^2_{\Delta\nu}(T) = 2f_0^2[R_{\dot{\tau}}(0) - R_{\dot{\tau}}(T)] \tag{7}$$

and depends only on the lag time T. Note that as T increases from zero to a lag time for which $R_{\dot{\tau}}(T) = 0$, $\sigma^2_{\Delta\nu}$ increases from zero to twice the variance of the difference in received frequency from the transmitted frequency.

The phase rate coherence time is defined in this work to be the lag time T_{NB} such that $\sigma_{\Delta\nu}$, the standard deviation of the change in received frequency, is equal to the bin width $1/T$. It is given implicitly here as the solution to

$$\sigma_{\Delta\nu}(T_{NB}) = f_0\sqrt{2[R_{\dot{\tau}}(0) - R_{\dot{\tau}}(T_{NB})]} = 1/T_{NB}. \tag{8}$$

Under the assumptions of a Garrett-Munk internal wave field and geometric acoustics, the travel time and its derivative will be a zero mean stationary Gaussian process. In Sec. IV, WPRM theory is applied to CZ propagation in the Philippine Sea to numerically compute $R_{\dot{\tau}}(T)$ and the phase rate coherence time T_{NB} defined by Eq. (8) over an ensemble of internal wave realizations.

IV. BACKGROUND PROFILE FOR EXPERIMENT

This section analyzes CZ propagation for the experiment with a smooth background profile. Ray trace results provide a picture of the propagation paths involved in CZ propagation. Formulas from WPRM with internal wave statistics are applied to the experiment profile to obtain the strength and diffraction parameters as well as the phase rate coherence time T_{NB} for a Garrett-Munk internal wave field.

Salinity and temperature profiles from 18 CTD casts made during the experiment are subsampled onto a depth grid with 50 m spacing and averaged. Spline fits to the coarse-grid averaged profiles provide smooth background profiles of salinity and temperature suitable for ray tracing. An additional point at 70 m depth is included in the coarse depth grid to prevent the spline from overshooting at the abrupt change in temperature slope at the onset of the thermocline. The CTD casts show a consistent mixed layer depth of 50 m throughout the experiment. The average salinity and temperature profiles are used to compute the "background" sound speed profile (SSP) $c_0(z)$, potential density profile $\sigma_0(z)$, and Brunt-Väissälä frequency profile $N_0(z)$.[13] These profiles are shown in Fig. 2. The background sound speed potential gradient $\mathrm{d}c_{pot}/\mathrm{d}z$ is also computed using these profiles.[7]

A. Background eigenrays and arrivals

The CZ predicted by the smooth background SSP from a source at 150 m depth is shown in Fig. 3. It shows that the start of the CZ occurs at 58 km range for a receiver at 150 m depth. Two caustics form a boundary around the CZ in the sense that a receiver will cross-these caustics as it transits through the CZ at a given fixed depth or as it leaves the CZ by moving to the surface. The first caustic is formed by rays with a downward (toward the seafloor) launch angle. These rays turn at great depth and turn around again at the caustic near the surface. The second caustic is formed by rays with an upward (toward the surface) launch angle. This caustic is at a slightly greater range than the first caustic.

As a receiver moves out in range within the CZ, these two caustics are associated with four possible eigenrays: a ray on its way to either caustic that comes in from below, and a ray coming down from either caustic above. The receiver depth and range determines which of these four possible eigenrays actually exist. Examining Fig. 3, a sample receiver at 160 m depth, between 57.5 and 58.5 km has two eigenrays arriving from below on their way to the two caustics. At 58.5 km, the arrival on its way to the first caustic drops out, and two close arrivals come from both caustics above. At 60 km, only a single arrival from the second caustic arrives from above.

B. Strength and diffraction parameters Φ and Λ

Using the smoothed profiles from the experiment shown in Fig. 2, the strength and diffraction parameters Φ and Λ are computed for all (non-bottom-interacting) eigenrays from a source at 150 m depth to a receiver at 150 m depth

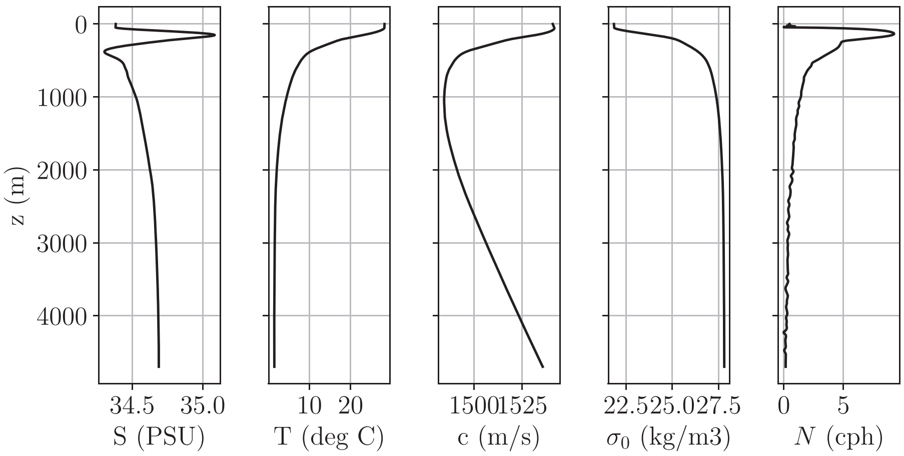

FIG. 2. Background profiles obtained by averaging CTDs from the experiment. The profiles are smoothed by sampling the mean CTD profile on a coarse 50 m depth grid and using spline interpolation. The smooth profiles are used for calculating eigenrays and internal wave modes necessary to compute the strength and diffraction parameters and the coherence time T_{NB} defined in Eq. (8).

and within the CZ at ranges of 58, 59, and 60 km representative of the various possible CZ eigenray paths. Eigenrays with their Fresnel zones for an example range of 59 km are shown in Fig. 4. Appendix B contains the details of the calculations. The standard deviation of sound speed perturbations due to a Garrett-Munk internal wave field used in the calculation of Φ and Λ is shown in Fig. 5 and demonstrates high variability in the vicinity of ray turning points near the source and receiver. The range of Φ and Λ values for this set of eigenrays is shown in Table I. For nearly all eigenrays and source-receiver ranges, $\Lambda \ll 1$, $\Lambda\Phi < 1$, and $\Lambda\Phi^2 > \pi$, placing the propagation in the "partially saturated" regime.[10,14] The exception is at 1.5 kHz at 58 km, where $\Lambda\Phi^2 \approx \pi$ placing it on the border between the partially saturated and unsaturated regimes. Partial saturation is an important designation because the signal in this regime has a smoothly evolving phase over the time scales of the CZ source tow in this experiment.

C. Travel time statistics

In Sec. III, Eq. (8), the autocorrelation function of travel time rate of change $R_{\dot{\tau}}(T)$ is used to implicitly define a

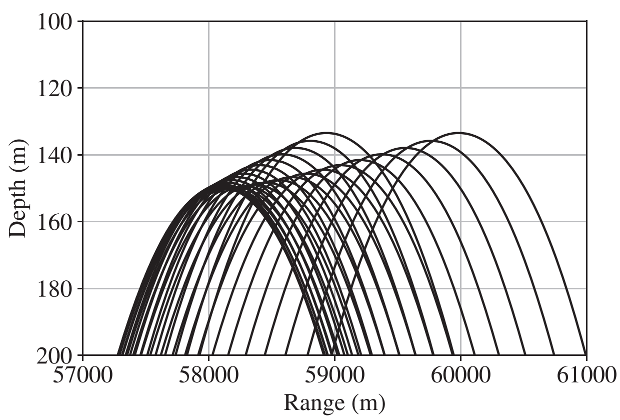

FIG. 3. Rays in the CZ for the smooth background sound speed profile with source depth 150 m. Launch angle spacing is 0.25°. Two caustics bound the CZ above and to either side. Eigenrays in the CZ either intersect the receiver on their way to the caustic, after turning at the caustic above, or along the caustic itself.

phase rate coherence time T_{NB}. We calculate $R_{\dot{\tau}}(T)$ using the methods in Ref. 15 applied to the smooth background profile relevant for the experiment at sample points $T_i = i \cdot (180\,\mathrm{s})$ for $i = 0, 1, \ldots, 6$ (the maximum lag time is 18 min, selected to safely exceed T_{NB}). The details of the calculation are presented in Appendix C. A linear interpolation approximation to $R_{\dot{\tau}}(T)$ is used to solve Eq. (8) for T_{NB} over the range of source frequencies in the experiment.

Table I shows the range of values from these calculations for eigenrays at 58, 59, and 60 km receiver ranges and with the source and receiver depths at 150 m. The predicted phase rate coherence time T_{NB} in the CZ for the experiment is approximately 1000 s at 1.5 kHz and 500 s at 5.5 kHz.

V. FULL WAVE SIMULATION

Thus far, all calculations apply to a single propagation path and a stationary source and receiver. In the experiment, there is a moving source and multiple arrivals. This section presents a single time-varying, range-dependent simulation spanning 19 min with a 5.5 kHz source in order to assess, in a simple and limited manner, the effect of multipath interference caused both by the fluctuating ocean as well as horizontal motion through the waveguide.

A. Sound speed perturbation simulation

An *ad hoc* hybrid approach for SSP simulation combining linear internal waves for dynamics and horizontal correlations with synthetic fine structure in the thermocline provides profiles for simulations consistent with the CTD measurements from the experiment.

The approach simulates fine structure within 20 m layers of water using the method of Pinkel[11] in the water column from 100 to 300 m depth. An example of synthetic fine structure is compared to the CTDs of the experiment in Fig. 6. The 20 m layers of water are then advected and strained by a larger scale internal wave field using $J = 20$ modes and the Garrett-Munk spectrum with mode cutoff parameter $j_* = 3$ and energy parameter $E_0 = 4$ to produce a time- and range-dependent SSP. The details are provided in Appendix D.

https://doi.org/10.1121/10.0032359

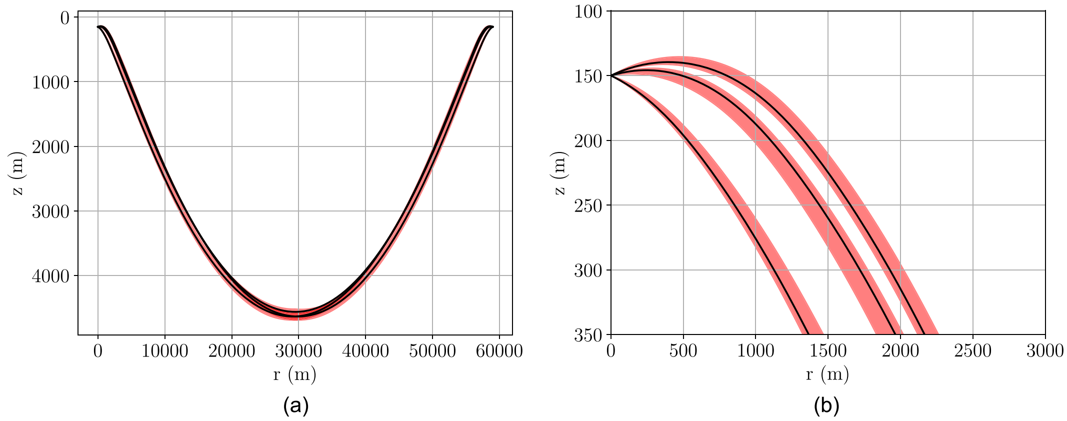

FIG. 4. (Color online) Rays and Fresnel zones at 5.5 kHz for CZ eigenrays at 59 km range. (a) Full eigenray paths from source to receiver both at 150 m depth. The eigenrays are purely refracted. (b) Eigenray paths within 3 km of the source. All eigenrays have at least one turning point in the thermocline (the downward launching ray here has a turning point near the receiver).

B. Simulation results

The simulation uses the background profiles from Fig. 2 and the method described in Appendix D to generate a time- and range-dependent SSP driven by internal wave field evolution and including fine structure such as that shown in Fig. 6. The range-dependent profile is sampled each minute for nineteen minutes (twenty samples). For each sample, the split-step parabolic equation[16] with a modal starter is used to solve for the pressure field from a 150 m deep 5.5 kHz source on a mesh with vertical spacing 0.0682 m and horizontal spacing 1.36 m.

The field intensity from the first time sample of the simulation output is shown in Fig. 7 with the four locations selected for analysis superimposed. Though the fine structure and internal wave effects in the SSP used for simulation complicate propagation compared to ray predictions using the smooth background profile from Sec. IV, the main CZ features are visible in the field. In particular, the simulation intensity field shows the caustics formed by rays with positive and negative launch angles at the source. The downgoing rays at the source associated with the CZ caustic closest to the source are generally unaffected by the fine structure. The upward-going rays at the source have a turning point in the fine structure near the source and therefore are perturbed off the smooth background paths. These rays form the more diffuse caustic located around 140 m depth and 59 km range.

The complex time series for the four labeled points are shown in Fig. 8 along with the received frequency minus the source frequency. It is seen that the phase evolves smoothly over the full nineteen-minute segment. Figure 8 also shows the phase in the beam of maximum amplitude using an 8 m aperture VLA centered on each selected point and indicates that the phase in a beam evolves similarly to its evolution at a single point in the CZ. This is interesting because the single point measurement contains contributions from multiple arrivals.

The phase rate $\dot{\phi}(t)$, estimated with a finite difference approximation, gives the received instantaneous frequency $\Delta f(t) = \dot{\phi}(t)/2\pi$ for each of the four points, as well as for the beam of maximum amplitude using an 8 m VLA. The time T required for the received frequency to change from its value at the start of the simulation by the bin width $1/T$ is between 500 and 600 s for all four points for the 5.5 kHz source. The frequency starts to change more rapidly around 400 s into the simulation after which the time T for the

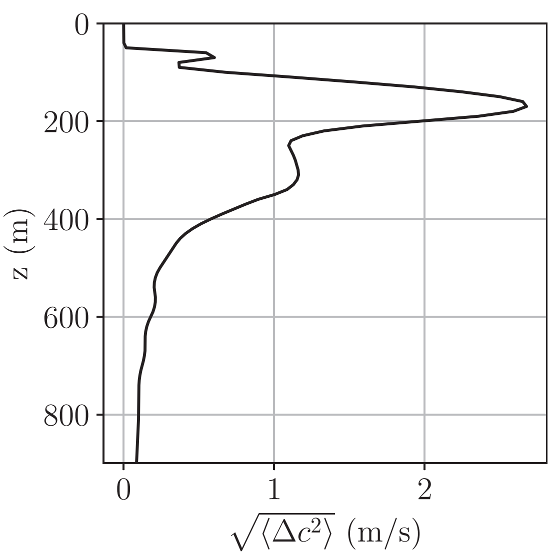

FIG. 5. The standard deviation of Garrett-Munk internal wave induced sound speed perturbations to the smooth background profile as a function of depth. There is high variability in the vicinity of the source and receiver depths and at the eigenray turning points for CZ propagation.

TABLE I. The range (minimum and maximum values) of strength and diffraction parameters as well as the range of phase rate coherence time T_{NB} defined in Eq. (8) for 1.5 and 5.5 kHz for all (non-bottom interacting) eigenrays at ranges of 58, 59, and 60 km using the background profile in Fig. 2. The parameter values place propagation in the partially saturated regime.

f (Hz)	Φ	Λ	$\Lambda\Phi$	$\Lambda\Phi^2$	$T_{NB}(s)$
1500	[37, 55]	$[8, 52] \times 10^{-4}$	$[3, 29] \times 10^{-2}$	[3, 16]	[922, 1300]
5500	[134, 201]	$[3, 22] \times 10^{-4}$	$[6, 43] \times 10^{-2}$	[9, 83]	[452, 603]

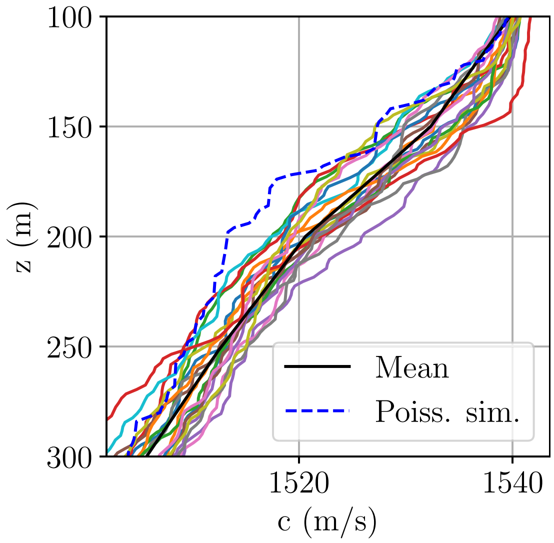

FIG. 6. (Color online) Comparison of an example Poisson generated sound speed profile (blue dashed) to CTD casts (color) from the experiment. A Poisson perturbation, generated with the method of Ref. 11 for depths between 100 m and 300 m, is advected by a range- and time-dependent internal wave field to perform an acoustic simulation in Sec. V.

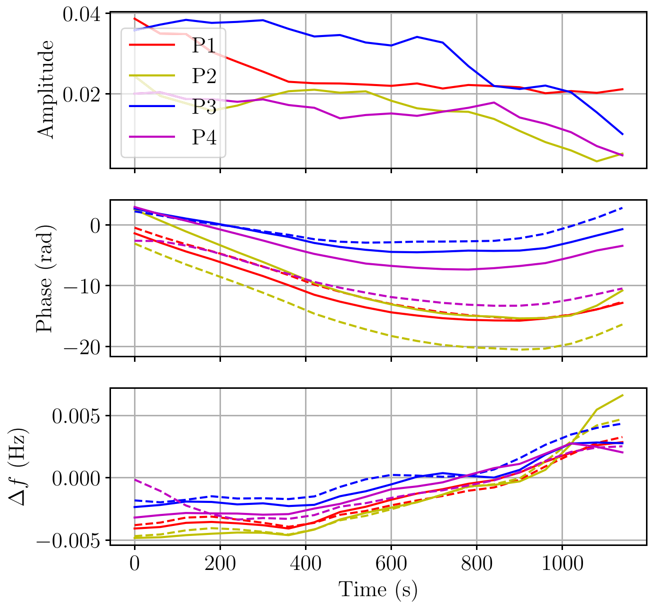

FIG. 8. (Color online) (Top) Amplitude of the simulated field from a 5.5 kHz stationary source at four selected CZ points shown in Fig. 7. (Middle) Phase of the simulated field at the four points (solid line) as well as in a beam (dashed line) from an 8-m VLA centered on each of the four points. (Bottom) The received frequency minus the source frequency at the point locations (solid lines) as well as in a beam (dashed line). The lag time T required for the received frequency to change by the bin width $1/T$ depends on the initial time and is between 300 and 600 s for the nineteen simulated minutes shown here.

frequency to change by $1/T$ is between 300 and 400 s. This time is approximately the same for the frequency change in a beam. Although a single realization cannot validate the statistical definition of phase rate coherence time T_{NB} in Eq. (8), the values from the simulation are on the order of $T_{NB} \approx 500$ s from WPRM theory shown in Table I.

The modeled pressure field in the range-dependent SSP from the first simulation time sample is used to gain a sense of the scale of multipath interference effects due to constant range-rate motion through the CZ (the data contains transmissions from a moving source). Figure 9 shows the amplitude and phase in the broadside beam of an 8 m VLA centered at 150 m depth at evenly spaced ranges throughout the CZ, simulating data from a constant range-rate source through a "frozen ocean." The phase is broken into 300 m segments, corresponding to the approximate range traversed by the source in the experiment during 5 min narrowband transmissions, and the linear portion of phase over these segments is removed. Figure 9 shows that the non-linear portion of the phase in the beam is less than 1/3 radian over 300 m segments within the high amplitude parts of the CZ. The phase of a single receiver at 150 m depth, also shown in Fig. 9, demonstrates larger non-linear phase excursions (up to 1 radian) compared to phase in the horizontal beam.

In summary, the simulation uses a 5.5 kHz source at 150 m depth and includes fine structure, internal wave driven ocean variability, and multipath interference due to changing source-receiver range. Single receiver measurements were compared to beamformer outputs from an 8 m VLA. For a stationary source and receiver in the presence of internal wave driven ocean changes, the phase in a beam closely resembles the phase at a single point. The simulation phase rate coherence time between 300 and 600 s at 5.5 kHz for a stationary source-receiver configuration is on the order of $T_{NB} \approx 500$ s predicted by WPRM theory and shown in Table I. For a source moving at constant range-rate, phase in a beam varies from a linear evolution by less than 1/3 radian over segments of 300 m within the high amplitude portion of the CZ.

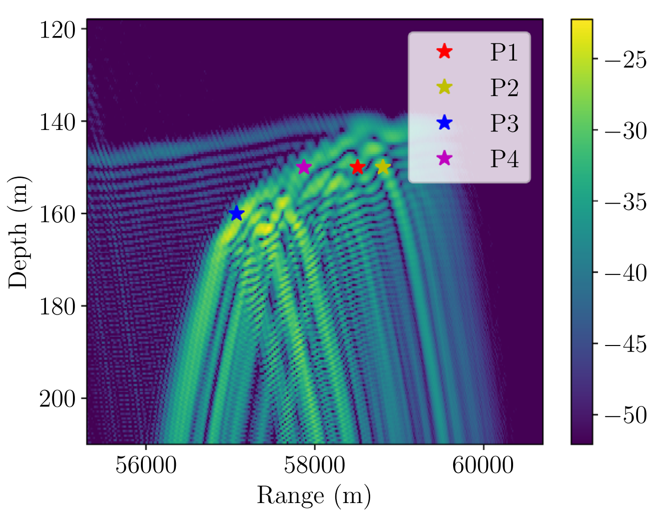

FIG. 7. (Color online) Intensity field of PE simulation in dB at 5.5 kHz at $t = 0$. The CZ stands out as a region of high intensity. Four points selected for time series analysis are shown as labeled stars.

VI. DATA ANALYSIS

This section presents analysis of the 5.5 kHz signal measured during a source tow in a CZ. Non-uniform

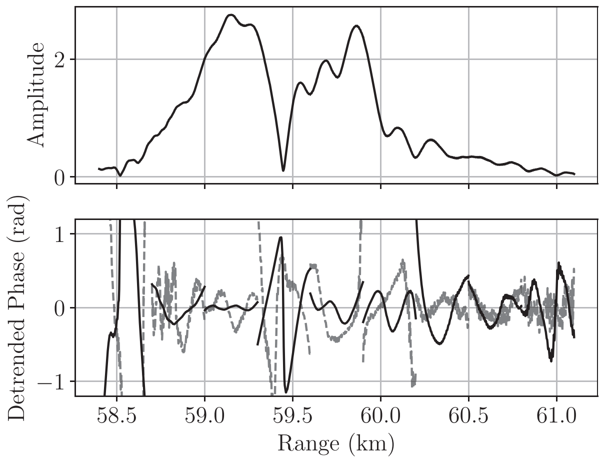

FIG. 9. (Top) Simulated amplitude in the horizontal beam of an 8 m VLA centered at 150 m depth with a static range-dependent SSP and 150 m depth source. (Bottom) Simulated phase in the horizontal beam of subsequent 300 m segments with the linear trend of that segment removed (solid black). The phase of the single receiver at the center of the VLA is also shown (dashed gray). Four high amplitude 300 m segments in the CZ demonstrate phase excursions of less than 1/3 radian (20 degrees) for the beamformed output and less than around 1 radian for a single receiver.

horizontal source motion is the dominant feature of the received signal phase. Measurements of source depth by a pressure sensor mounted on the source tow body can be related to the source tow excursions from its mean linear range evolution. For all CZ segments of data of length 120 s, these pressure sensor measurements are highly correlated with the nonlinear component of phase measured in a broad horizontal beam. For certain segments, the match continues up to 210 s. This relationship can be used to accurately correct for non-uniform motion effects on segments up to 210 s. The DFT is applied to data segments of increasing length and increasing SNR is observed for segments up to 128 s.

A. Transmission overview

During the source tow, an ITC-1007 source transmitted a repeating 300 s comb of sinusoidal signals followed by 300 s of broadband transmissions. The intensity and arrival pattern for the CZ at 5.5 kHz are shown in Fig. 10, which demonstrates seven 300 s segments of received signal numbered 1 through 7. Of these segments, Segments 3 through 7 were used for analysis due to their good signal-to-noise ratio (SNR). All data timestamps are shown in seconds since JD117 2019 01:53:20 UTC.

B. Signal processing

For the band of interest, the measured pressure field is band-shifted by the nominal Doppler shifted frequency f_r for a 1 m/s closing source. The band-shifted data is low-pass filtered and decimated in stages: three stages of decimation by a factor of 8 and 1 stage of decimation by a factor of 4 to arrive at a final sampling rate of $25\,000/2048 \approx 12.2$ Hz. Each stage applies an anti-aliasing Chebyshev infinite impulse response (IIR) low pass filter before decimating. The IIR filter, though generally not linear phase, has nearly linear phase over the band of interest. The final passband is around 10 Hz, or ± 5 Hz, centered at the nominal Doppler shifted frequency for a 1 m/s range-rate.

The simulation indicates that beamforming has a limited effect on phase rate coherence time. Nonetheless, the signal-to-noise ratio improvement obtained by beamforming is necessary for the phase analysis presented here. This analysis uses conventional beamforming. Phase is measured in a broad horizontal beam, as the goal is simply surface noise rejection as opposed to isolation of a single propagation path.

C. Comparison of phase and pressure sensor measurement

The simulation indicates a nearly linear phase response (with small $<1/3$ radian deviations) to horizontal movement within the CZ. Under this assumption, there exists a horizontal wavenumber k such that the signal phase ϕ nearly evolves according to

$$\phi(t) = \phi_0 + \omega_0 t - k r(t), \tag{9}$$

where ω_0 is the source frequency in rad/s and $r(t)$ is the source to receiver range. Decompose the source-receiver range $r(t)$ into a uniform component related to the mean range-rate v and a residual component $\delta r(t)$ so that

$$r(t) = vt + \delta r(t) \tag{10}$$

and

$$\phi(t) = \phi_0 + (\omega_0 - kv)t - k\delta r(t). \tag{11}$$

The residual component of motion $\delta r(t)$ consists of both short time scale excursions that are related to the ship heave in response to swell as well as longer time scale excursions related to departures of the ship speed from its mean speed v.

Measurements of source depth from a pressure sensor on the source tow body can be used to estimate $\delta r(t)$ because the source tow body is connected to the ship by a cable under tension. The array motion contribution to $\delta r(t)$ is assumed to be negligible, as GPS measurements of the buoy position indicate small, nearly linear movement during the 300 s source transmission segments. For short time scale excursions, the source is constrained to move along the catenary of the tow cable approximated by the tangent line at the tow body, providing a linear relationship between short time scale change in the *demeaned* pressure $\delta z(t)$ and short time scale excursions in the residual range $\delta r(t)$,

$$\delta r_{short}(t) = \frac{1}{\tan\theta}\delta z(t), \tag{12}$$

where θ is the tangent line inclination with respect to the horizontal. Over longer time scales, the source tow body responds to a change in the ship speed by equilibrating to a

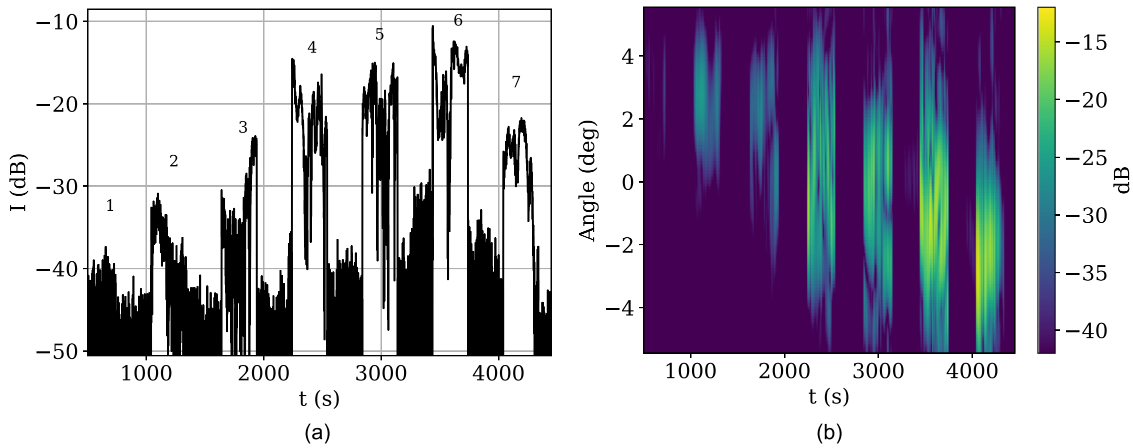

FIG. 10. (Color online) (a) Intensity in a broad horizontal beam at 5.5 kHz in a CZ with seven labeled segments of sinusoidal transmissions. Segments 3 to 7 have sufficient SNR for a careful analysis of phase. (b) Beamformer output (magnitude squared) at 5.5 kHz in a CZ. Positive angle corresponds to an arrival coming in from above the array. The arrival pattern is similar to the predicted pattern for a receiver moving right (back end of CZ) to left (front of CZ) through the rays in Fig. 3 from around 61 to 58 km at a depth of around 150 m.

different depth. Therefore, the slowly varying component of δz provides a measurement of the relative ship speed (the mean displacement $\delta z = 0$ being associated with the mean speed v). Assuming a linear relationship between the demeaned source depth δz and the ship speed deviation from its mean value, the longer time scale excursions of δr from its mean track vt due to changes in ship speed will be proportional to the *integral* of δz,

$$\delta r_{long}(t) = D \int \delta z(t) \mathrm{d}t, \tag{13}$$

where D is the source depth response to a change in speed. Taking these two observations together quantifies the relationship between δr and δz,

$$\delta r(t) = \frac{1}{\tan\theta} \delta z(t) + D \int \delta z(t) \mathrm{d}t. \tag{14}$$

The accuracy of Eq. (14) will degrade if the catenary angle θ is time varying, when the tow cable length is manually adjusted to maintain a nominal depth of 150 m, or due to nonlinearity in the equilibrium source depth response to ship speed.

Equipped with the relationship between the demeaned pressure sensor measurements of source depth δz and the residual component of source range δr, we perform a least squares fit of the samples of unwrapped phase $\phi(t_i)$ at the sampling rate after decimation in a broad horizontal beam in order to estimate the values a, b, c, and d in the discretized model

$$\phi(t_i) = a + bt_i + c\delta z(t_i - \hat{\tau}) + d\Delta t \sum_{k=0}^{i} \delta z(t_k - \hat{\tau}) \tag{15}$$

for various segment lengths of data [we have approximated the integral in Eq. (14) with a simple Riemann sum]. Here, $\hat{\tau}$ is an estimate of the acoustic travel time necessary to obtain the pressure measurement at the time of transmission. It was manually tuned, and the least squares fit was seen to be insensitive to the exact value used within 1 s precision. The estimated parameters physically represent $a = \phi_0$, $b = \omega_0 - kv$, $c = -k/\tan\theta$, and $d = -kD$. By using an approximate horizontal wavenumber of $k = \omega_0/c_0$ for source frequency ω_0 rad s^{-1} and $c_0 = 1500$ m/s, the mean range-rate is obtained from b as $v = k^{-1}(\omega_0 - b)$ and the catenary angle is obtained from c as $\theta = \arctan(-k/c)$. For simplicity, the noise on each measurement is assumed to be independent and of equal variance.

The results of least squares fitting is shown in Fig. 11 for segments 5 and 7 (refer to Fig. 10 for segment labels). For these two segments, the first 210 s of data are used to fit the pressure sensor model in Eq. (15) and to obtain estimates of a,b, c, and d. The fit degrades substantially for longer segments of data.

The residuals of the two fits shown in Fig. 11 display the component of the phase that cannot be fit by the model in Eq. (15). It demonstrates a periodic component with a period of approximately 7 s and an amplitude of around 2 radians. This periodic component, isolated with a high pass filter, is highly correlated with the high pass filtered pressure sensor measurement, indicating that it is related to the ship heave. The remaining, slower varying residual phase has an amplitude around 2 radians, which is larger than the nonlinear phase variations seen in the simulation due to multipath interference with range (estimated to be less than 1/3 radian) and a time-varying medium.

Model fits to shorter segments of 60 s provide a series of parameter estimates and allow for an examination of their variability with time. Parameter estimates from these shorter segment fits estimate a mean range-rate $v = -1.04 \pm 0.04$ m/s. The estimated catenary angle θ varies between 54° and 70° with respect to the horizontal and changes by less than 5° from one minute to the next. The model assumes a constant catenary angle for any given data segment, which is one potential source of model mismatch.

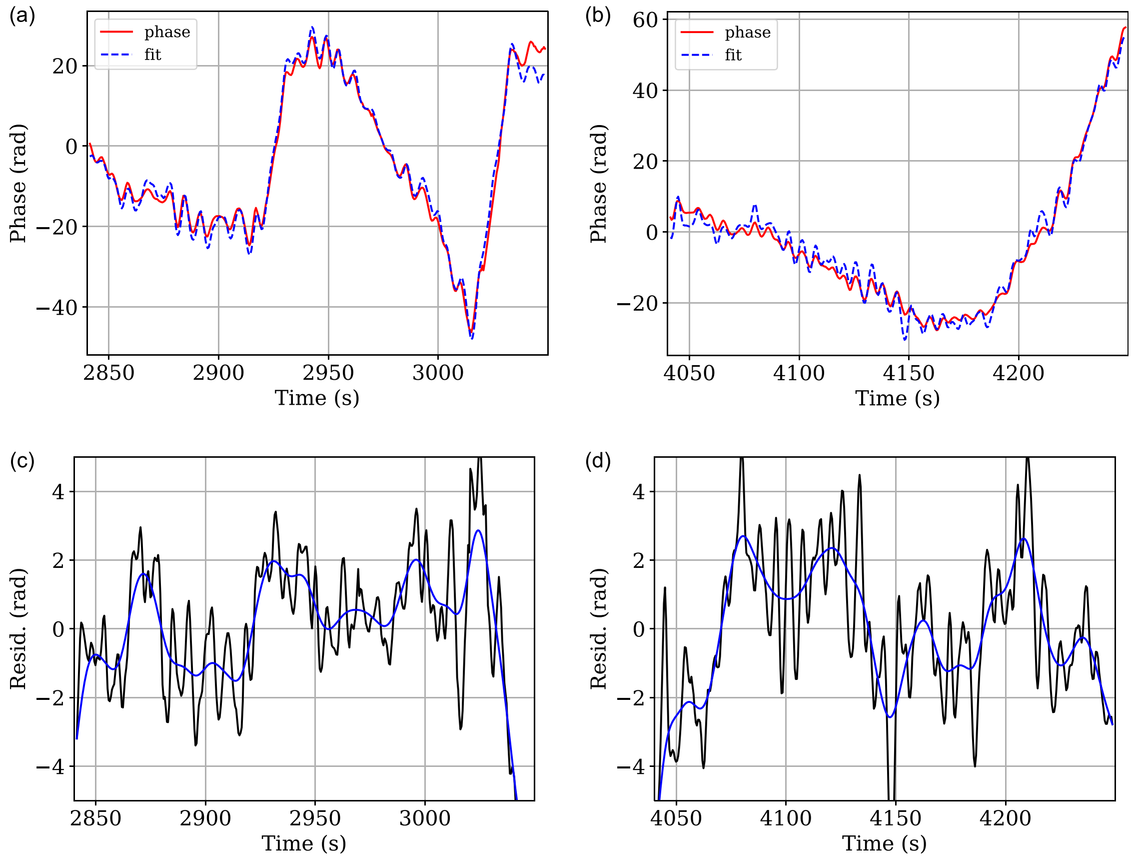

FIG. 11. (Color online) Top: Phase measured in a broad horizontal beam at 5.5 kHz with its linear trend removed (red) compared to the least squares fit from the pressure sensor measurements of source depth variation (blue dashed) for 210 s sub-segments of data for segment 5 (left) and segment 7 (right) of the CZ. The phase evolution is highly correlated with the pressure sensor measurements of source depth. Bottom: The residuals from the least squares fit for the panels directly above (black) as well as the residuals shown after a low pass filter removes the 7 s period signal (blue). The 7 s component in the residual was seen to be highly correlated with the high-pass filtered pressure sensor measurement of source depth variation.

D. Gain from coherent integration

This section examines the limits of coherent integration of the signal with a DFT from the source tow transmissions measured in a broad horizontal beam in the CZ.

The complex basebanded data consist of a signal component $s[i]$ plus a noise component $w[i]$,

$$x[i] = s[i] + w[i]. \tag{16}$$

Section III considers a sinusoidal signal with a random frequency modulation. To maintain simplicity of presentation and solidify the basic concepts, we assume here that the signal component consists of a deterministic complex basebanded sinusoidal signal whose frequency is at the center of a DFT bin and that the noise component is assumed to be a realization of a zero-mean complex white Gaussian noise process with variance σ_w^2. The length N DFT of the data is defined as

$$X_N[k] = \sum_{i=0}^{N-1} x[i]e^{-j(2\pi k/N)i} \tag{17}$$

and is the sum of the DFT of the signal component $S_N[k]$ and the DFT of the noise component $W_N[k]$,

$$X_N[k] = S_N[k] + W_N[k]. \tag{18}$$

Note that from our assumption that the signal is a complex sinusoid at a DFT bin center, the input signal power $P_s = A^2$ where A is the signal amplitude and the signal power in a DFT bin, $|S_N(k)|^2$ is $N^2A^2 = N^2Ps$. From our assumptions on the noise process, the expected value of input noise power P_n is equal to the noise variance σ_w^2 and the expected value of noise power in a DFT bin, $\langle |W_N[k]|^2 \rangle$, is $N\sigma_w^2 = NP_n$.

The signal-to-noise ratio (SNR) is defined as the ratio of signal power to noise power. Thus, at the input $SNR_{in} = P_s/P_n$. In a length N DFT bin, the output SNR is

$$SNR_{out}(N) = \frac{|S_N[k]|^2}{NP_n}. \tag{19}$$

Given our assumptions on the signal, $SNR_{out}(N) = N^2Ps/NPn = NPs/Pn = NSNR_{in}$. Thus, for a perfectly coherent complex sinusoid with frequency corresponding to a length N DFT bin center, SNR_{out} increases linearly with respect to N.

It is useful to focus on the normalized signal DFT power. Define the quantity $R(N)$ to be the ratio of the signal DFT power divided by DFT length squared, $|S_N[k]|^2/N^2$, to the input signal power P_s,

$$R(N) = \frac{|S_N[k]|^2/N^2}{P_s}. \tag{20}$$

The increase in SNR, SNR_{inc}, expressed as the ratio of SNR_{out} in a DFT bin to the input $SNR_{in} = P_s/P_n$ in decibels, can be written in terms of $R(N)$ as

$$10\log_{10}SNR_{inc}(N) = 10\log_{10}R(N) + 10\log_{10}N. \tag{21}$$

For the complex basebanded tonal signal with a frequency matched to the DFT bin center considered here, $R(N) = 1$ and $SNR_{inc}(N) = N$. For an input sinusoidal signal whose frequency does not coincide with a DFT bin center, scalloping loss will cause a decrease in up to a few dB in the value of $R(N)$[17] and, accordingly, $SNR_{inc}(N)$. Due to its finite bandwidth, the sinusoidal signal with random frequency modulation considered in Sec. III can be over-resolved by the DFT (i.e., the DFT bin does not capture a majority of the input signal power), resulting in a value of $R(N) < 1$.

Data is divided into sub-segments of length $T = 1$ s ($N = 12$) to $T = 256$ s ($N = 3125$), and Eq. (21) is averaged over sub-segments. As described in Sec. VI, the pressure sensor fit to phase for each sub-segment provides an estimate of the non-uniform source motion effect on phase. The data can be corrected for non-uniform source motion by removing the predicted phase $\hat{\phi}$ from the pressure sensor measurement of source depth variation [Eq. (15)]. This is accomplished by multiplying the input time series by $e^{-i\hat{\phi}(t)}$ before applying the DFT. The results are shown in Fig. 12 for both corrected and uncorrected data at 5.5 kHz. SNR_{inc} is seen to plateau at a segment length of 128 s. SNR_{inc} in the uncorrected data increases by around 8 dB for a DFT integration time increase from 1 s to 128 s, while SNR_{inc} for the corrected data increases by around 13 dB.

VII. CONCLUSION

The phase rate coherence time is defined as the time T_{NB} over which the standard deviation of the *change* in a randomly evolving received frequency equals the DFT bin width $1/T_{NB}$. Results from WPRM theory are used to compute the phase rate coherence time T_{NB} for CZ propagation when the changing received frequency is driven by sound speed perturbations along the ray paths from a Garrett-Munk internal wave field. For the deep water Philippine Sea experiment described here, the expected narrowband phase rate coherence time in the CZ, predicted by WPRM theory, is $\sim$500 s at 5.5 kHz (in the absence of source motion). A single simulation of CZ propagation at 5.5 kHz in a time- and range-dependent SSP over nineteen minutes indicates smoothly varying phase and a narrowband phase rate coherence time consistent with WPRM predictions. Mid-frequency (5.5 kHz) data from a CZ source tow demonstrates that the non-linear component of the phase evolution in a beam is highly correlated with pressure sensor measurements of source depth variation for segments of data up to 210 s. The received signal at 5.5 kHz in a CZ could be coherently integrated for up to 128 s after correcting for source motion.

ACKNOWLEDGMENTS

This research was supported by the Office of Naval Research (ONR) under Grant No. N00014-23-1–2557. Dave Ensberg helped with data access. Rob Pinkel provided helpful discussions of SSP fine structure and his simulation method.

AUTHOR DECLARATIONS

Conflict of Interest

The authors have no conflicts to disclose.

DATA AVAILABILITY

The acoustic data are available from W. Hodgkiss, subject to sponsor restrictions.

APPENDIX A

The WPRM literature traditionally defines coherence in terms of the mutual coherence function[15,18]

$$\Gamma(x_1, x_2, T) = \langle p^*(x_1, t+T)p(x_2, t)\rangle, \tag{A1}$$

where $p(x, t)$ is the complex pressure field at a point x and time t with any time dependent source phase removed, $(\cdot)^*$ denotes complex conjugation, and $\langle\cdot\rangle$ denotes expectation over ensembles of medium realizations (e.g., internal wave induced sound speed perturbations). In Eq. (A1), the field is assumed to be stationary. The coherence time at a given point x is then defined in terms of the MCF as the "characteristic length" of the complex degree of temporal coherence γ,[12]

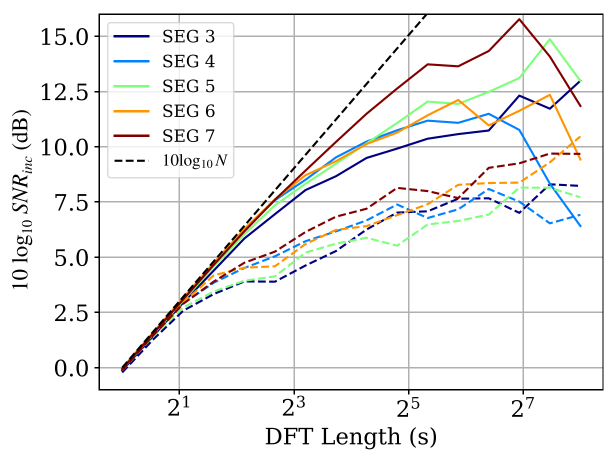

FIG. 12. (Color online) SNR_{inc} in DFT bin of maximum magnitude for varying DFT length for uncorrected data (dashed line) and data corrected for source motion (solid line) at 5.5 kHz. Corrected data uses the predicted phase from source depth measurements and least squares coefficient estimates in Eq. (15) to simulate what one may expect to measure from a moving source at constant range-rate. The model degradation that occurs around 128 s creates the precipitous drop in SNR_{inc} for the corrected data. The black dashed line indicates theoretical gain for a sinusoidal signal whose frequency is at a DFT bin center.

$$\gamma(x,x,T) = \frac{\Gamma(x,x,T)}{\sqrt{\Gamma(x,x,0)^2}}, \tag{A2}$$

which has a modulus between 0 and 1.

The MCF can be written in terms of the phase structure function[18,19]

$$D(T) \equiv \langle[\phi(t+T) - \phi(t)]^2\rangle \tag{A3}$$

as

$$\Gamma(T) = \exp\left[-\frac{1}{2}D(T)\right], \tag{A4}$$

where ϕ is the phase of the acoustic field and the pressure field has been normalized to unity in the absence of any perturbations. The coherence time is therefore seen to be related to the growth of the phase structure function with increasing lag time T.

For the purposes of coherently summing broadband transmissions sent at separate times this is a natural definition. For small values of $D(T)$, the phase is expected to remain approximately constant and coherent summation is possible. As $D(T)$ increases with T to a value of π^2, it becomes increasingly unlikely that the transmissions will remain in phase with one another and coherent summation will fail to provide gain. However, from the perspective of narrowband integration with a DFT, a change in the absolute phase presents no issue as long as it occurs linearly (i.e., as long as the phase rate is constant). A linear change in phase with time simply corresponds to a constant shift in received frequency. Therefore, the phase rate coherence time defined in Eq. (8) is better suited to quantify the integration time of a narrowband signal with a DFT than the coherence time from the MCF.

APPENDIX B

The formulas from Colosi[14] used to compute the strength and diffraction parameters are reproduced here,

$$\Phi^2 = q_0^2 \int_\Gamma ds \langle\mu^2(z)\rangle L_p(\theta, z), \tag{B1}$$

$$\Lambda = \frac{q_0^2}{\Phi^2} \int_\Gamma ds \langle\mu^2(z)\rangle L_p(\theta, z) \frac{\{m^2\} R_f^2(s)}{2\pi} \tag{B2}$$

with the following notation:

(1) $c_0 = 1500$ m/s is a reference sound speed.
(2) ω_0 is the source angular frequency.
(3) $q_0^2 = \omega^2/c_0^2$ is a reference horizontal wavenumber.
(4) Γ denotes the path of the ray under consideration.
(5) s is the ray coordinate $\mathrm{d}s/\mathrm{d}r = (\tan\theta)^{-1}$ with θ the local grazing angle and r range.
(6) $\langle\mu^2(z)\rangle = \langle\Delta c(z)^2\rangle/c_0^2$ is the expected relative sound speed perturbation, with expectation taken over all internal wave realizations consistent with the Garrett-Munk spectrum. See the following paragraph for the description of the relationship between sound speed perturbations and internal wave displacement.
(7) $L_p(\theta, z)$ is the correlation length (units of distance) of the sound speed perturbations at depth z along a tangent line with angle θ and is given as Eq. (3) in Ref. 14.
(8) $R_f(s)$ is the vertical Fresnel zone about the ray at point s. It is defined as follows. Choose a point S with coordinates $z(s), r(s)$ along the eigenray under consideration. The eigenray has travel time T. Fix a point P vertically displaced by a distance $\Delta z > 0$ from S. Compute two new eigenrays. The first connects the source to P and the second connects P to the receiver. Now compute the sum of the two eigenrays' travel times and call it $T(P)$. The Fresnel zone $R_f(s)$ is the displacement distance $\Delta = |S - P|$ such that the travel time difference $T(P) - T_0$ corresponds to a phase shift of π from the unperturbed ray. Since Δz may differ for displacements above and below the ray, a more precise definition is $R_f(s) = \Delta z^+ + \Delta z^-$, where the superscripts indicate the orientation of vertical displacement from the ray. The difference in Δz^+ and Δz^- is evident in Fig. 4.
(9) $\{m^2\}$ is the average vertical wavenumber squared. The WKB approximation directly relates the local buoyancy profile $N(z)$ to vertical wavenumber. The Garrett-Munk spectrum controls the distribution between modes. An approximate value suitable for our application is accordingly[14]

$$\{m^2\} = \left(\frac{\pi N(z)}{N_0 B}\right)^2 \frac{\langle j\rangle}{\langle j^{-1}\rangle}, \tag{B3}$$

where $\langle j\rangle = \Sigma H(j)j$ and $\langle j^{-1}\rangle = \Sigma H(j)j^{-1}$ gives the mode weighting prescribed by the Garrett-Munk spectrum. $N_0 B = \int_0^D N(z)\mathrm{d}z$ with D equal to water column depth [this notation is a holdover from the exponential stratification model considered by Garrett and Munk where $N(z) = N_0 e^{-z/B}$].
(10) π is the ratio of the circumference of a circle to its diameter.

Following Ref. 7, sound speed perturbations are related to an internal wave displacement field $\zeta(\vec{x}, t)$ by advecting the sound speed potential gradient $\mathrm{d}c_{pot}/\mathrm{d}z$ estimated from the background profile

$$\Delta c(\vec{x}, t) = \frac{\mathrm{d}c_{pot}}{\mathrm{d}z} \zeta(\vec{x}, t). \tag{B4}$$

With this assumption,

$$\langle\mu^2(z)\rangle = \frac{1}{c_0^2}\left(\frac{\mathrm{d}c_{pot}}{\mathrm{d}z}(z)\right)^2 \langle\zeta^2(z)\rangle. \tag{B5}$$

For the calculation of Φ^2 and Λ, $\langle\zeta(z)^2\rangle$ is computed using the Garrett-Munk spectrum energy density $E_0 = 4000\,\mathrm{J\,m^{-2}}$ and characteristic mode number $j_* = 3$. A formula for the maximum mode number corresponding to an internal wave

https://doi.org/10.1121/10.0032359

field with unlikely shear instability is given in Eq. (18) of Ref. 14 in terms of the buoyancy profile. For the buoyancy profile relevant to our experiment, the value of J is approximately 600. The expected displacement variance depends only on depth due to the assumptions of horizontal isotropy and stationarity of the internal wave field.

Note that in order to complete the calculation of Λ and Φ, one only needs the smooth background salinity and temperature profiles, as well as the longitude and latitude of the experiment. Given these quantities, one can then compute: (1) the potential density $\sigma_0(z)$, (2) the sound speed $c_0(z)$, (3) the adiabatic temperature gradient $\mathrm{d}c_{(pot)}/\mathrm{d}z$, (4) buoyancy profile $N(z)$, (5) the internal wave modes $\zeta_{j\kappa}(z)$ and frequencies $\omega_{j\kappa}$, (6) the displacement correlation function $\langle\zeta(z)\zeta(z')\rangle$, (7) correlation length $L_p(\theta,z)$, (8) the background eigenrays and Fresnel zones, and finally (9) the integral expressions (B1) and (B2).

APPENDIX C

In geometric acoustics the travel time for sound along a ray path Γ through the dynamic sound speed profile $c(x,z,t) = c_0(z) + \Delta c(x,z,t)$ is

$$\tau(t) = \int_\Gamma \left(c_0(z) + \Delta c(x,z,t)\right)^{-1} \mathrm{d}s. \tag{C1}$$

For $\Delta c \ll c$, this is approximately equal to

$$\tau(t) = \tau_0 - \int_\Gamma \frac{\Delta c(x,z,t)}{c_0(z)^2} \mathrm{d}s, \tag{C2}$$

where τ_0 is the travel time for the ray through the smooth background profile $c_0(z)$.

The first time derivative of τ is given by

$$\dot{\tau}(t) = -\int_\Gamma \frac{\mathrm{d}\Delta c(x,z,t)}{\mathrm{d}t} c_0^{-2}(z) \mathrm{d}s. \tag{C3}$$

By assuming a linear relationship between the sound speed perturbation Δc and internal wave displacement as in Eq. (B4), the time dependence of the sound speed perturbation is given by

$$\frac{\mathrm{d}c(\vec{x},t)}{\mathrm{d}t} = \frac{\mathrm{d}c_{pot}}{\mathrm{d}z}\dot{\zeta}(\vec{x},t), \tag{C4}$$

where $\dot{\zeta}$ is the vertical velocity of the internal wave field.

Because the amplitudes of the internal waves in the Garrett-Munk field are assumed to be zero-mean Gaussian random variables, $\dot{\tau}(t)$ is a zero-mean stationary Gaussian process and is completely described by the autocorrelation function $R_{\dot{\tau}}(T) = \langle\dot{\tau}(t+T)\dot{\tau}(t)\rangle$. Applying Eqs. (C3) and (C4), we obtain $R_{\dot{\tau}}(T)$,

$$R_{\dot{\tau}}(T) = \int_\Gamma\int_\Gamma \frac{\frac{\mathrm{d}c_{pot}}{\mathrm{d}z}(z)\frac{\mathrm{d}c_{pot}}{\mathrm{d}z}(z')\langle\dot{\zeta}(\vec{x},t)\dot{\zeta}(\vec{x}',t+T)\rangle}{c_0^2(z)c_0^2(z')}\mathrm{d}s\mathrm{d}s'. \tag{C5}$$

The above equation can be used to compute the expected phase rate coherence time in Eq. (8) for a given source frequency, ray path, and background profile.

The correlation function $\langle\dot{\zeta}(\vec{x},t)\dot{\zeta}(\vec{x}',t+T)\rangle$ was computed Garrett-Munk spectrum parameters energy density $E_0 = 4000\,\mathrm{J\,m^{-2}}$ and mode number roll-off $j_* = 3$, and a horizontal wavenumber mesh from 0.0035 to 0.5 cpkm.[20]

The correlation function is saved on a grid with a 1 km spacing in the separation range and 10 m spacing in depth and approximated by linear interpolation to evaluate the integral in Eq. (C5) for lag times $T=0$ to $T=18$ min. The maximum mode number J was varied between 20 and 600 and seen to have an insignificant effect on the value of $R_{\dot{\tau}}(T)$. This makes sense considering that from the internal wave dispersion relation, high order modes have a smaller frequency and vertical velocity than the low order modes; they also have a smaller weight in the Garrett-Munk spectrum compared to the low order modes.

APPENDIX D

This appendix describes the steps used to generate synthetic sound speed profiles with range-dependence, dynamics, and the step-like fine structure seen in CTD casts. The approach perturbs a coarse grid of isopycnals with mean depth $\{\bar{Z}_i\}$ and mean separation $\{\bar{Z}_{i+1} - \bar{Z}_i\} = 20$ m with a Garrett-Munk internal wave field. It also perturbs a fine grid of isopycnals in the thermocline from 100 to 300 m with mean separation of 2 m and mean depth $\bar{z}_{i,j}$ given relative to the coarse isopycnal depth $\bar{Z}_i$ directly above using the Poisson method of Pinkel.[11] With this notation, the isopycnal associated with the fine grid mean depth $\bar{z}_{i,j}$ has a mean depth $\bar{Z}_i + \bar{z}_{i,j}$. The isopycnals at their mean depths have a temperature $T(\bar{Z}_i + \bar{z}_{i,j})$ and practical salinity $S(\bar{Z}_i + \bar{z}_{i,j})$.

The ocean state is characterized by the instantaneous isopycnal depths $\nu_{i,j}(x,t) = Z_i(x,t) + z_{i,j}(x,t)$, where Z_i is the instantaneous depth of the ith coarse isopycnal determined solely by the internal wave field and $z_{i,j}$ is the depth *referenced to* Z_i of the jth fine isopycnal in the ith coarse layer (see Fig. 13 for a schematic).

The internal wave modal equation using $N(z)$ for the experiment is solved on a grid of horizontal wavenumber κ between 0.001 and 0.5 cpkm for modes $J = 1,\ldots,20$. The numerical approach is detailed in Richard Evans' memorandum.[21] This produces the vertical modes $\zeta_j(z;\kappa)$ and their frequencies. The modes are randomly excited using the Garrett-Munk spectrum to produce a displacement field in the plane between source and receiver $\zeta(x,z,t)$ using the Cartesian approach as in Ref. 20. The internal wave field displaces the coarse grid of isoypycnals with mean depths $\bar{Z}_i$ to perturbed depths $Z_i(x,t) = \bar{Z}_i + \zeta(x,\bar{Z}_i,t)$.

Each 20 m layer between two isopycnals on the coarse grid is divided into finer layers with a mean thickness of $\Delta\bar{z} = 2$ m. The 2 m layer of water separating each pair of adjacent isopycnals is a "Poisson element." A random fine structure realization for a single 20 m layer is obtained by independently drawing a strain for each Poisson element

https://doi.org/10.1121/10.0032359

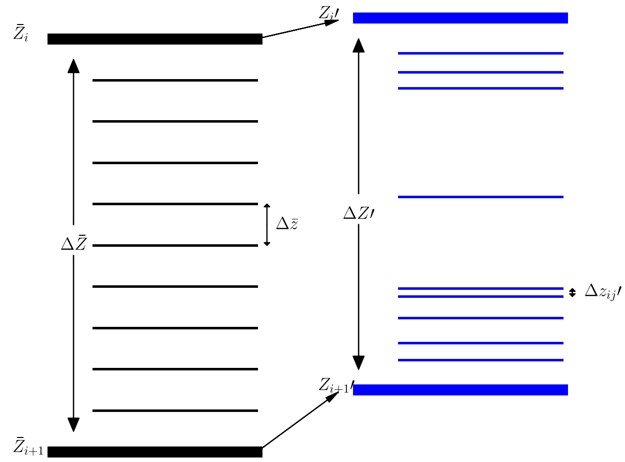

FIG. 13. (Color online) Schematic of isopycnal perturbation. Mean isopycnal depths are on the left in black. Perturbed depths are shown on the right in blue. The thick blue lines are displaced by the internal wave field from $\bar{Z}_i$ to $Z_i' = \bar{Z}_i + \zeta(\bar{Z}_i, x, t)$. The fine isopycnals within the segment have a Gamma distributed separation $\Delta z_i'$ and are referenced to the upper isopycnal Z_i'.

$\Delta z_i/\Delta\bar{z} \sim \mathrm{Ga}(\kappa_0, 1/\kappa_0)$ from a Gamma distribution with parameter κ_0. The strain of the last Poisson element is selected so that the mean strain within the layer is 1. In the event that the last element does not fit within the 20 m layer, then the strains are redrawn. In this work we use $\kappa_0 = 0.8$ (determined by fit to the CTD data). The result is a collection of fine structure isopycnal depths $\{z_{ij}\}$, where i indexes the coarse 20 m thick layer and j indexes the fine Poisson element interfaces.

To combine the two, the isopycnal depths, *relative to the bounding coarse isopycnal* Z_i are given from the strains by a cumulative sum, defined recursively as $z_1 = \Delta z_1$, $z_j = \Delta z_j + z_{j-1}$. By referencing the fine isopycnal grid to the coarse grid, the thermocline fine structure is advected by the internal waves (which act on the coarse grid).

To summarize, a set of fine structure strains is generated for each layer in a set of 20 m thick layers of water between 100 and 300 m depth. A coarse grid of 20 m separated isopycnals is displaced by the internal wave field. The result is a distortion of the original 2-m spacing isopycnal grid. A schematic is shown in Fig. 13.

The perturbed sound speed profile is obtained by calculating the sound speed at each depth $Z_i + z_{ij}$ using the salinity $S(\bar{Z}_i + \bar{z}_{ij})$ and *in situ* temperature $T(\bar{Z}_i + \bar{z}_{ij})$ associated with that isopycnal. The *in situ* temperature change due to adiabatic expansion with changing pressure is computing using $\Delta T = (\mathrm{d}T/\mathrm{d}z)(\bar{Z}_i + \bar{z}_{ij})(\bar{Z}_i + \bar{z}_{ij} - Z_i - z_{ij})$. The sound speed profile at these perturbed depths is then linearly interpolated back onto a uniform grid with spacing $\Delta\bar{z} = 2$ m.

[1]F. Hale, "Long-range sound propagation in the deep ocean," J. Acoust. Soc. Am. **33**(4), 456–464 (1961).
[2]R. Urick and G. Lund, "Coherence of convergence zone sound," J. Acoust. Soc. Am. **43**(4), 723–729 (1968).
[3]K. P. Bongiovanni, W. L. Siegmann, and D. S. Ko, "Convergence zone feature dependence on ocean temperature structure," J. Acoust. Soc. Am. **100**(5), 3033–3041 (1996).
[4]C. Chen, "Effect of environment dependence of convergence zones in the tropical and subtropical sea areas of western pacific," in *2016 IEEE/OES China Ocean Acoustics (COA)* (2016), pp. 1–5.
[5]E. C. Bhatt, A. B. Baggeroer, and R. A. Weller, "Overflow waters in the western Irminger Sea modify deep sound speed structure and convergence zone propagation," J. Acoust. Soc. Am. **155**(2), 1216–1229 (2024).
[6]L. A. Chernov, *Wave Propagation in a Random Medium* (Dover, New York, 1960).
[7]W. H. Munk and F. Zachariasen, "Sound propagation through a fluctuating stratified ocean: Theory and observation," J. Acoust. Soc. Am. **59**(4), 818–838 (1976).
[8]V. I. Tatarskiĭ and R. A. Silverman, *Wave Propagation in a Turbulent Medium* (Dover, New York, 1967).
[9]V. I. Tatarskiĭ, *The Effects of the Turbulent Atmosphere on Wave Propagation* (Israel Program for Scientific Translations, Jerusalem, 1971).
[10]J. A. Colosi, *Sound Propagation through the Stochastic Ocean* (Cambridge University Press, New York, 2016).
[11]R. Pinkel, "The Poisson link between internal wave and dissipation scales in the thermocline. Part I: Probability density functions and the Poisson modeling of vertical strain," J. Phys. Oceanogr. **50**(12), 3403–3424 (2020).
[12]A. Derode and M. Fink, "The notion of coherence in optics and its application to acoustics," Eur. J. Phys. **15**(2), 81–90 (1994).
[13]Intergovernmental Oceanographic Commission, "The international thermodynamic equation of seawater, 2010: Calculation and use of thermodynamic properties" (2010).
[14]J. A. Colosi, "A reformulation of the Λ-Φ diagram for the prediction of ocean acoustic fluctuation regimes," J. Acoust. Soc. Am. **137**(5), 2485–2494 (2015).
[15]S. M. Flatté, R. F. Dashen, W. H. W. H. Munk, K. M. Watson, and F. Zachariasen, *Sound Transmission through a Fluctuating Ocean*, Cambridge Monographs on Mechanics and Applied Mathematics (Cambridge University Press, Cambridge, 1979).
[16]F. D. Tappert, *The Parabolic Approximation Method* (Springer, Berlin, 2005), pp. 224–287.
[17]F. Harris, "On the use of windows for harmonic analysis with the discrete Fourier transform," Proc. IEEE **66**(1), 51–83 (1978).
[18]S. A. Reynolds, S. M. Flatté, R. Dashen, B. Buehler, and P. Maciejewski, "AFAR measurements of acoustic mutual coherence functions of time and frequency," J. Acoust. Soc. Am. **77**(5), 1723–1731 (1985).
[19]R. Dashen, S. M. Flatté, and S. A. Reynolds, "Path–integral treatment of acoustic mutual coherence functions for rays in a sound channel," J. Acoust. Soc. Am. **77**(5), 1716–1722 (1985).
[20]K. B. Winters and E. A. D'Asaro, "Direct simulation of internal wave energy transfer," J. Phys. Oceanogr. **27**(9), 1937–1945 (1997).
[21]R. Evans, "Calculation of internal wave eigen-frequencies and modes; Displacement and sound speed realizations," Memorandum, SAIC (2000), https://oalib-acoustics.org/website_resources/Other/wave/Wave.pdf (Last viewed 6/5/2024).